IEEE Access
Multidisciplinary | Rapid Review | Open Access Journal

Received 20 May 2022, accepted 14 June 2022, date of publication 23 June 2022, date of current version 28 June 2022.

Digital Object Identifier 10.1109/ACCESS.2022.3185048

Design, Analysis, and Control of a Multilink Magnetic Wheeled Pipeline Robot

MINGZE GAO, MIN HUANG, KAI TANG, XUQIANG LANG, AND JIAMING GAO
School of Mechanical and Electrical Engineering, Beijing Information Science and Technology University, Beijing 100192, China

Corresponding author: Min Huang (huangmin@bistu.edu.cn)

This work was supported in part by the Science and Technology Project of Beijing Science and Technology Commission under Grant Z191100001419009.

ABSTRACT This paper presents a multi-link magnetic wheeled pipeline robot (PR-I), which is a flexible and modular robotic mechanism. It is designed for inspection, cleaning or disinfection of central air conditioning ventilation duct. PR-I can adapt to complex pipeline terrain, and move in the ventilation ducts freely. A novel magnetic wheel is proposed for wall climbing, which is circumferentially embedded with rectangular permanent magnets. Firstly, the wall climbing model is established to obtain the adsorption conditions, then the effects of the magnetizing direction of the magnets, magnetic wall thickness and gap on the magnetic force are analyzed by finite element method. Finally, the optimal magnetic wheel structure is obtained through dynamic simulation analysis. The motion control of the robot is carried out in an embedded system. Two fuzzy controllers based on ranging sensor and IMU are proposed for straight motion and turning motion, and gait sequences are designed for obstacle surmounting. The performance of the robot was evaluated in a real ventilation duct. The experimental results show that PR-I has good trafficability and control performance in various terrains.

INDEX TERMS Pipeline robot, structural design, magnetic wheel, motion control.

I. INTRODUCTION

Ventilation ducts are widely used in the central air conditioning system and fresh air system of large buildings. In order to ensure air quality, regular inspection and disinfection are necessary. Ventilation ducts installed in large areas are multi-branch topological structures. A simple schematic diagram is shown in Figure 1. The ducts are usually rectangular with a diameter of 100mm-400mm and a thickness of 0.5mm-2mm. There are many complex terrains such as T-branches, bend pipes, steps, and vertical pipelines in the ducts. Therefore, researchers are committed to developing various forms of pipeline robots to replace humans [1]–[6]. At present, some commercial air-conditioning pipeline robots are mostly 4-wheel or crawler equipment, but the obstacle surmounting ability is weak and cannot cope with vertical ducts. Modular multi-link robots have gradually become a research hotspot because they have higher mobility, flexibility, and a stronger ability to adapt to the terrain. Kakogawa *et al* proposed a multi-link articulated wheeled robot [7]–[10]. Each joint of the robot was installed with a torsion spring, which made the robot passively adapt to the pipe wall. The robot could be clamped on the inner wall of the pipe in an M-shaped or V-shaped posture, and resulting clamping force allowed the robot to climb vertically. However, the clamping force will decrease gradually as the pipe diameter increases, so the wheels may slip.

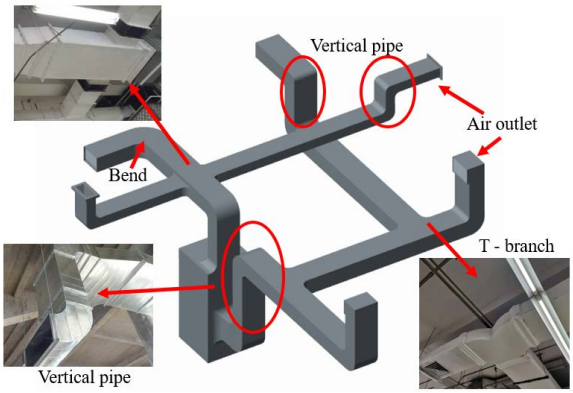

FIGURE 1. Schematic diagram of ventilation pipeline environment.

In [11], Ye *et al* designed a cross elastic support mechanism to actively provide clamping force, and the pressure was controllable, but the size of the robot was large and the moving speed was slow. Dertien *et al* proposed a

The associate editor coordinating the review of this manuscript and approving it for publication was Mohammad Alshabi.

multi-link pipeline robot with two sets of V-shaped clamping structures [12]. The V-shaped mechanism was composed of two links at the head and tail of the robot, and the middle part was designed as a rotating module to generate rotation around itself, so it could turn in multiple directions. In [13], Yan *et al* designed a pipeline plugging robot, and its supporting structure was composed of three groups of wheels evenly distributed at 120° in the circumferential direction. It could climb straight pipes with slopes up 37°. Similar robot structures are described in references [14]–[16]. Generally speaking, the vertical climbing of this kind of robot is realized by clamping force, so it is more suitable for pipes with a small diameter or little change in pipe diameter. In a ferromagnetic environment, magnetic adsorption is another effective climbing method, including electromagnetic adsorption and permanent magnetic adsorption [17]–[19]. Permanent magnetic adsorption is more energy efficient, and it can avoid adsorption failure caused by accidental power outage. Some robots climb the wall by installing permanent magnetic adsorption devices (PMAD), and this is non-contact adsorption. There is a certain gap between the permanent magnet adsorption device and the wall. Yan *et al* designed a PMAD composed of permanent magnets arranged in different magnetizing directions, and it was installed at the bottom of the robot [20]. Tavakoli *et al* installed the magnets and magnetic suction cup around each driving wheel [21]. Compared with direct contact, the magnetic force is reduced, but its action area is much larger, so it still has a good adsorption effect. However, PMAD usually has a large size and needs enough space for installation. Magnetic wheels and tracks are usually magnets themselves or carry magnets, which can simplify the structure and save space. The coaxial installation of ring magnet and yoke or steel rim is a common magnetic wheel structure [22]–[26]. The magnetic circuit of the wheel is optimized, so the magnetic wheel has a large adsorption force. In some studies, the ring magnets were rearranged in segments with Halbach array [27], [28], and the magnetic force was further enhanced. But at the same time, the separation of magnetic wheel and pipe wall is not easy. In [29], Park *et al* proposed a tracked climbing robot, which was composed of three separable modular units, and the permanent magnets were distributed on the track of each unit. The cooperation of multiple modules could cope with some complex terrain, such as perpendicular wall-to-wall transitions. These findings show that the modular magnetic adsorption robot is a better solution to deal with the complex terrain of ventilation ducts.

In this study, we proposed a multi-link magnetic wheeled pipeline robot called PR-I. It can move in the ventilation ducts freely, and has the ability of wall climbing and obstacle surmounting. We developed a modular structure and shape design, which is composed of head, middle unit, and tail. It can arbitrarily increase or decrease the number of modules to achieve fast switching and flexible matching of different tasks. We proposed a novel magnetic wheel and carried out some simulations to analyze the magnetic force. We built a principle prototype and developed the control system. The control algorithms and strategies were designed according to different pipeline terrains. Finally, the motion performance was verified by experiments in the ventilation ducts.

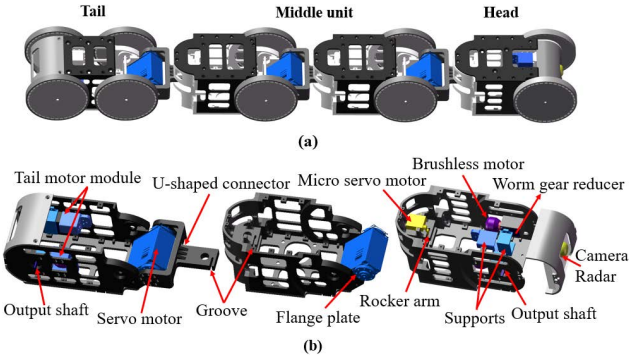

FIGURE 2. CAD model of PR-I robot. (a) Assembly model. (b) Internal details.

II. MECHANICAL DESIGN

PR-I consists of head, tail, and two middle units, as shown in Figure 2. Two adjacent units are connected by a 2-DOF U-shaped mechanism, which can realize the pitch motion and yaw motion. The pitch joints of PR-I are controllable and driven by the servo motor. The range of motion is $-90°$ to $90°$. The yaw joint can be locked and free, which is achieved by a micro servo motor and rocker arm. The micro servo motor positions the rocker arm into the grooves of the body and the U-shaped connector, and the yaw joint is locked. When the robot needs to turn, rotate the rocker arm out to unlock the yaw joint. The forward power of the robot is provided by the motor units of the head and tail.

The head of PR-I is the function module, with installation hole and electrical interface reserved, which can carry brush, sensor, cleaning and inspection equipment, etc. A camera and a TOF array laser radar module are installed at the front of the head for navigation. Disinfectant can also be carried inside the body to disinfect the pipeline through the spraying device. The motor modules are installed on the machine body through supports. The power output of the motor is transmitted to the output shaft through the worm gear reducer, and PR-I can realize self-locking when stationary. The magnetic wheels provide additional adsorption force, which improves the driving capability. It not only realizes wall climbing, but also ensures the stability of the robot when changing its posture. The battery and some control circuit boards are installed inside the middle unit, and the wheels are driven wheels. The tail of PR-I is the communication module. The signal shielding in the pipeline is serious, so cable communication is the best choice. Optical fiber communication is adopted because of its large transmission capacity and good quality, and some communication interface circuits, micro switchboard, and optical fiber transceiver are arranged in the tail.

PR-I is currently designed as four units. In fact, if only the motion function is needed, the head and tail units can

also meet the current pipeline environment. However, the final robot needs to mount detection equipment or cleaning equipment, and a multi-link modular design can achieve more functions. The first two units or more of the robot can be regarded as a simple manipulator. The head can be positioned by changing posture of the robot through the angle control of the pitch joint. The comprehensive observation and inspection of the ventilation pipe can be realized by using the camera or inspection equipment installed on the head. We built the robot platform and realized the motion function, which will be beneficial to the subsequent research in other aspects. A physical prototype is shown in Figure 3. The body material is aluminum alloy. In order to increase the friction coefficient between the wheel and the pipe wall, the magnetic wheel was covered with rubber film. Some main technical specifications are shown in Table 1.

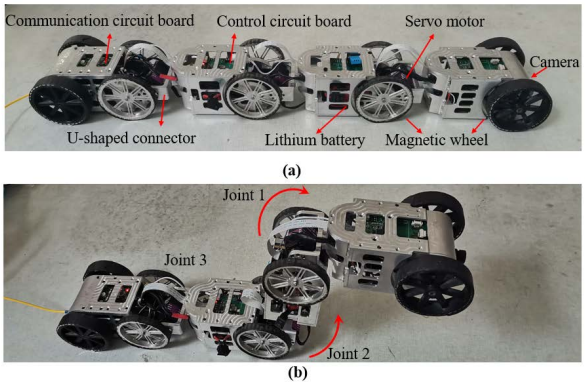

FIGURE 3. Physical prototype. (a) Initial posture. (b) Change the posture.

TABLE 1. Main technical specifications.

Specification	Value
Total length	0.62m
Width	0.08m
Head weight	0.46kg
Unit 2 weight	0.45kg
Unit 3 weight	0.46kg
Tail weight	0.71kg
Wheel radius	0.035mm
Battery	7.4V/4400mAh
Rated torque of pitch joint	5N·m
Motor rated power	40W

III. MEGNETIC WHEEL DESIGN AND ANLYSIS

Wall climbing is the most complex and most likely to fail in various movements. Designing a magnetic wheel that produces as much magnetic force as possible is usually the first consideration, which is necessary for wall climbing. However, when PR-I needs to change its posture, such as obstacle surmounting, too much magnetic force is undesirable. The head or the first two units need to be lifted, and the separation of the wheel from the pipe wall will be more difficult, which will consume more energy. When the magnetic force is too large to separate, the mechanical structure and electrical equipment will be damaged. Therefore, the magnetic force should be limited to a suitable range.

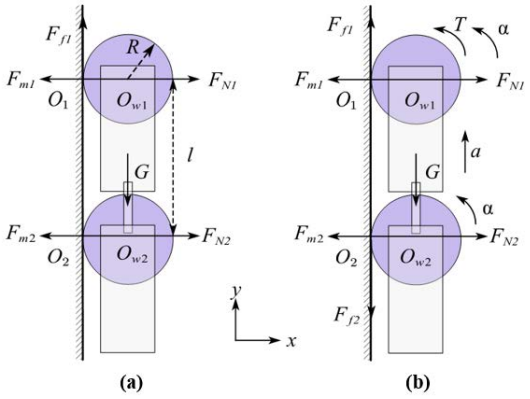

FIGURE 4. Force analysis of climbing wall. (a) Static. (b) Dynamics.

A. FORCE ANALYSIS OF WALL CLIMBING

Firstly, the mechanical model of wall climbing is analyzed. PR-I is required to be able to brake on the vertical pipes, and not slip and overturn when moving. Figure 4 describes statics and dynamics.

1) STATICS

Due to symmetry, one side of the first two units is taken as the research object, and the static analysis is shown in Figure 4(a). Where O_i is the contact point between the wheel and the pipe wall, and O_{wi} is the wheel center. R is the wheel radius. l is the distance between the centers of two wheels. The total mass is m and the total gravity is G. F_{fi} is the friction force between the wheel and the pipe wall, and F_{Ni} is the supporting force. The magnetic adsorption force is F_{mi}. The driving wheel can be self-locking, whereas the driven wheel is free, so when the robot is attached to the pipe wall, the friction is all provided by the driving wheel, and the friction of the driven wheel is zero. The equilibrium equation can be obtained as Equation (1). F_x, F_y are the resultant forces in the x and y directions. M_{O2} is the resultant moment of O_2.

$$\begin{cases} \sum F_x = F_{N1} + F_{N2} - F_{m1} - F_{m2} = 0 \\ \sum F_y = F_{f1} - G = 0 \\ \sum M_{O2} = F_{m1} l - F_{N1} l - GR = 0 \end{cases} \tag{1}$$

The condition that the robot remains stationary and does not slide on the pipe wall is that the friction force between the driving wheel and the pipe wall is less than or equal to the maximum static friction force. The condition that the robot does not overturn is that the support force is greater than zero. It can be denoted as:

$$\begin{cases} \mu F_{N1} \geq F_{f1} \\ F_{N1} \geq 0 \end{cases} \tag{2}$$

where μ is the friction coefficient, and combine Equation (1) and Equation (2), the condition for magnetic adsorption force is obtained as:

$$F_{m1} \geq \max \begin{cases} \dfrac{G\,(l+\mu R)}{\mu l} \\ \dfrac{GR}{l} \end{cases} \tag{3}$$

2) DYNAMICS

The dynamic analysis is shown in Figure 4(b). Where T is the driving torque of the motor. a is the acceleration of the robot's center of mass, and the angular acceleration of the wheel is α, which satisfies $a = \alpha R$. The moment of inertia of the wheel is J_i. According to D'Alembert's principle, it can be obtained as:

$$\begin{cases} \sum F_x = F_{N1} + F_{N2} - F_{m1} - F_{m2} = 0 \\ \sum F_y = F_{f1} - F_{f2} - G - ma = 0 \\ \sum M_{O2} = T + F_{m1}l - F_{N1}l - GR \\ \qquad\qquad - maR - J_1\alpha - J_2\alpha = 0 \end{cases} \tag{4}$$

For wheels:

$$\begin{cases} T - F_{f1}R = J_1\alpha \\ F_{f2}R = J_2\alpha \end{cases} \tag{5}$$

The constraint condition still satisfies Equation (2). When climbing the pipe wall, the relationship between the magnetic adsorption force and the motor torque is as follows:

$$\begin{cases} F_{m1} \geq \dfrac{1}{\mu R}\,(GR + maR + J_2\alpha) \\ \qquad\quad + \dfrac{1}{l}\,(GR + maR + J_1\alpha + J_2\alpha - T) \\ T \geq GR + maR + J_1\alpha + J_2\alpha \end{cases} \tag{6}$$

Numerically, the magnetic wheel is wrapped in rubber film, so the friction coefficient μ is 0.8. G is a quarter of the total gravity, and l is 0.13 m. According to Equation (3) and Equation (6), the condition that the robot can remain stationary or move stably at a uniform velocity in the vertical pipe is that the minimum magnetic force of each driving wheel is $F_m = 7.9$N and the minimum torque of the motor is $T = 0.182\,\text{N}\cdot\text{m}$.

B. FORCE ANALYSYS OF MAGNETIC WHEEL

In order to meet the requirements of lightweight and miniaturization, we proposed a novel permanent magnetic wheel. The rectangular permanent magnets are embedded in the wheel, as shown in Figure 5. NdFeB permanent magnet is selected in this study, which is a common permanent magnet material with a large magnetic energy product. This means that less material is needed to produce the same adsorption effect, which can make the permanent magnet smaller, so it is suitable to be embedded in the wheel. At present, rectangular permanent magnets with a size of 8mm × 4mm × 2mm are used. The material of the wheel hub is magnesium-aluminum alloy, which greatly reduces the mass of the wheel.

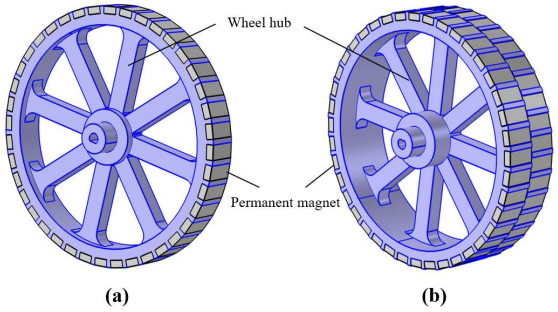

FIGURE 5. Magnetic wheel. (a) Single-row magnet structure. (b) Double-row magnet structure.

The original design proposed a single-row magnet structure as shown in Figure 5(a). The magnetic wheel is approximately in surface contact during the movement. The maximum magnetic force occurs when the rectangular magnet in the contact area is parallel to the pipe wall, as shown in Figure 6(a). When the rectangular magnet is tilted relative to the pipe wall, the magnetic force will decrease, as shown in Figure 6(b). In order to reduce the fluctuation of magnetic force, we improved the magnetic wheel and proposed a double-row magnet structure, and the two rows of magnets are staggered arrangement, as shown in Figure 5(b). When the magnets in one row of the contact area are tilted to the wall, the magnet in the other row is parallel, as shown in Figure 6(c), which can effectively reduce the change of magnetic force. In addition, the magnetic force is also enhanced.

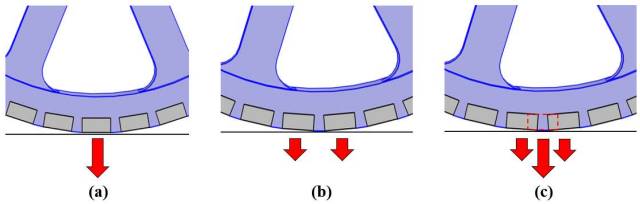

FIGURE 6. Magnetic force at different positions. (a) The rectangular magnet is parallel to the pipe wall. (b) The rectangular magnet is tilted relative to the pipe wall. (c) The magnets in one row of the contact area are tilted relative to the pipe wall, the magnet in the other row is parallel.

The driving wheels of PR-I (head and tail wheels) adopts the double-row magnet structure to ensure the stability of wall climbing. According to the force analysis in Part A, the friction of the driven wheel only makes the wheel rotate passively. Therefore, the magnetic force required for the driven wheel is not large. In order to reduce the weight, the driven wheel adopts the single-row magnet structure. In general, when the size and magnetization of the magnet are constant, the magnetic force of the magnetic wheel is mainly related to the magnetizing direction of the magnets, the thickness of the magnetic wall, and the gap between the magnetic wall and the wheel. Some analysis was carried out respectively. Firstly, we designed several arrangements with different magnetizing directions, as shown in the Figure 7.

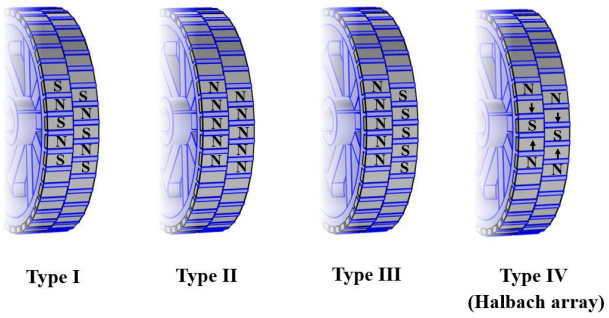

FIGURE 7. Magnetic wheels with magnets arranged in different magnetizing directions.

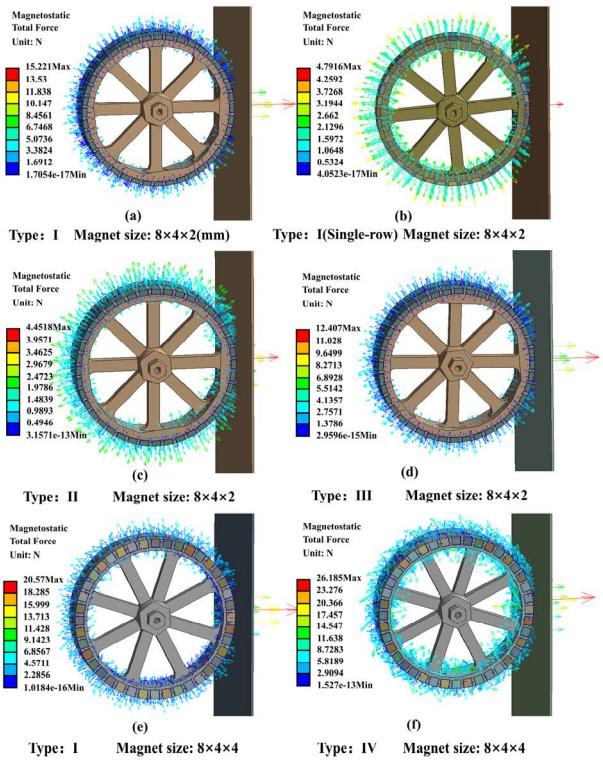

FIGURE 8. Magnetic adsorption force under different magnetic wheel structures.

The rectangular permanent magnet is magnetized along the thickness direction, so Type IV (Halbach array) magnets require a square section. The four magnetic wheels were analyzed by finite element method, and the magnetic simulation was carried out in ANSYS environment. The simulation parameters were set as follows: Residual magnetic induction intensity of magnet was $B_r = 1.28$ T, and coercive force $H_c = 9.4 \times 10^5$(A/m). The relative permeability of the magnetic wall was $\mu_r = 4000$, and the relative permeability of the air medium and the hub were set to 1. Firstly, the change of magnetic force under different magnetizing direction arrangements were analyzed. The results are shown in Figure 8, and the magnetic force is described by the total force.

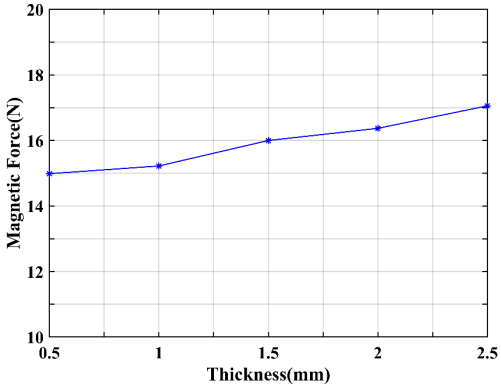

FIGURE 9. Relationship between magnetic force and thickness of magnetic wall.

It can be seen from Figure 8 (a) and (b) that the double-row structure can produce nearly three times the magnetic force of the single-row structure. By comparing Figure. 8 (a), (c) and (d), it can be concluded that the Type I arrangement produces the maximum magnetic force under the same magnet size. Figure 8(e) shows that when the magnet size changes to $8 \times 4 \times 4$, the magnetic force increases by 35%. At this size, Halbach array provides a greater magnetic force, as shown in Figure 8(f). In summary, the single-row structure and Type II wheel do not meet the magnetic force condition of the current robot driving wheel ($F_m > 7.9$), and Type IV (Halbach array) can produce maximum magnetic force.

The thickness change of magnetic wall and the gap can bring about the change of magnetic force, because it can also change the magnetic circuit. Figure 9 describes the magnetic force variation when the thickness of magnetic wall is in the range of 0.5-2.5mm (common thickness of ventilation duct). It can be seen that in this range, the increase of thickness can enhance the magnetic force, but changes little. The relationship between magnetic force and gap is shown in Figure 10. As the gap increases, the magnetic force decreases sharply. When the gap exceeds 3mm, the magnetic force is almost zero.

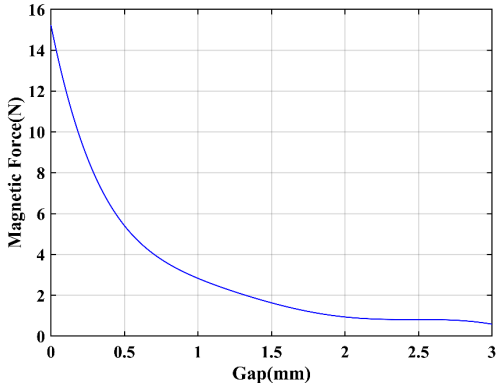

FIGURE 10. Relationship between magnetic force and gap.

C. DYNAMIC SIMULATION

In order to study the influence of magnetic force of magnetic wheel on motion performance, the dynamic simulation was performed in the environment of automatic dynamic analysis of mechanical systems (ADAMS). The CAD model of the robot was imported into ADAMS, and added motion pairs. The parts of the robot shell were connected through fixed pairs, and rotating pairs were added between the wheels and the robot body, then rotating pairs were also added at the pitch and yaw joints. The contact constraints between the wheels and the pipe wall were added. The static friction coefficient was set to 0.8, and the magnetic force is composed of force vectors. The model is shown in Figure 11. The magnetic force of the magnetic wheel was set to 4, 12, 15, 20, and 26N for wall climbing simulation respectively. Among them, when the magnetic force was set to 4N, the wheel slipped and the robot could not climb the vertical pipe wall. In other cases, wall climbing could be realized. The friction of the driving wheel in the simulation process is shown in Figure 12.

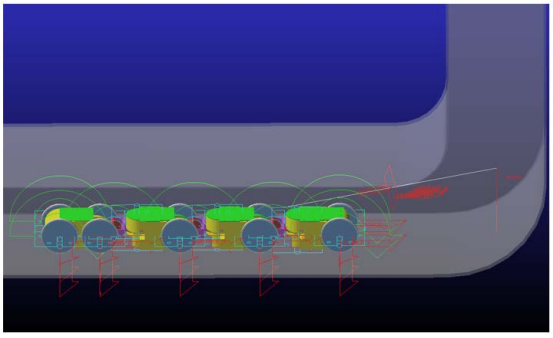

FIGURE 11. Simulation model of the robot.

Horizontal pipe and vertical pipe are usually connected by curved pipe. In simulation, when the robot began to transition from horizontal pipe to vertical pipe, the friction of the driving wheel increased gradually. When the four units were completely transitioned to the vertical pipe, the friction was stable around 4N to 5N. When the robot began to transition from the vertical pipe to the horizontal pipe, due to geometric constraints, it was not guaranteed that the wheels of each unit contact the pipe wall. The wheels of the middle unit might hang in the air, and the interaction among the units generated additional positive pressure on the driving wheels, so the friction became larger at this time. When the robot completely transited to the horizontal pipe, the friction decreased gradually. A comparison showed that when the magnetic force was 12N, the friction fluctuated greatly, and with the increase of magnetic force, the friction fluctuation gradually decreased. Therefore, a large magnetic force will significantly improve the stability of wall climbing.

Another simulation was carried out to study the pitch joint torque required to separate the magnetic wheel from the pipe wall under different magnetic forces, as shown in Figure 13. It can be seen that when the magnetic force of the magnetic wheel is greater than 17.5N, the required torque is greater than 5N·m, which exceeds the rated torque of the servo motor currently in use. Therefore, it is reasonable to adopt type III magnetic wheel under the current size. In fact, Type IV wheel can be optimized by reducing the size of magnet, which is the content of future research. The actual magnetic wheel is shown in Figure 14, and the magnetic force obtained by dynamometer is 13.9N. After covering the rubber film, the magnetic force decreased by 20%.

IV. CONTROL

A. CONTROL ARCHITECTURE

The control architecture of PR-I is shown in Figure 15, including upper application layer and bottom control layer. The upper application layer provides a man-machine interface, which can obtain information and send control instructions. Robot status, sensor data, and images are displayed on the operation interface and mobile monitoring terminal. The operator can use the handle to control the robot movement manually. The bottom control layer is an embedded system based on ARM microcontroller, which realizes hardware drive and control algorithm programming. The master-slave control mode is adopted, and the master controller is responsible for sensor data acquisition and processing, communication, and motion planning. The slave controller is responsible for driving the actuator, and the control form is position and speed control. The remote operation terminal communicates with the robot embedded system by establishing a local area network, and the optical fiber is used as the signal transmission medium. Client-server mode is adopted. The microcontrollers and camera module in the bottom control layer are used as the servers, and the upper application layer is used as the client. At the operation terminal, different devices (operation interface, handle or mobile devices) can be connected to different server addresses (controller or camera) to get the required data.

B. CONTROL STRATEGY

The internal environment of the ventilation duct is narrow, and manual control alone has poor reliability and low efficiency. We adopted a semi-automatic control strategy. The operator sends behavioral control instructions, such as turning or obstacle surmounting. In the robot embedded system, the master controller performs motion planning according to different terrains, and adjusts the output control quantity.

1) STRAIGHT MOTION

It was noticed that PR-I yawed as it moved in a straight line due to the poor synchronization of multi-unit motion. A fuzzy controller based on ranging sensor and IMU is proposed to improve the motion performance.

Figure 16 describes the robot posture in straight motion in the general case. θ is the yaw angle of the head, which is obtained by the IMU mounted on the head. Range sensors are installed on both sides of the head. $E_d = x_1 - x_2$ is the

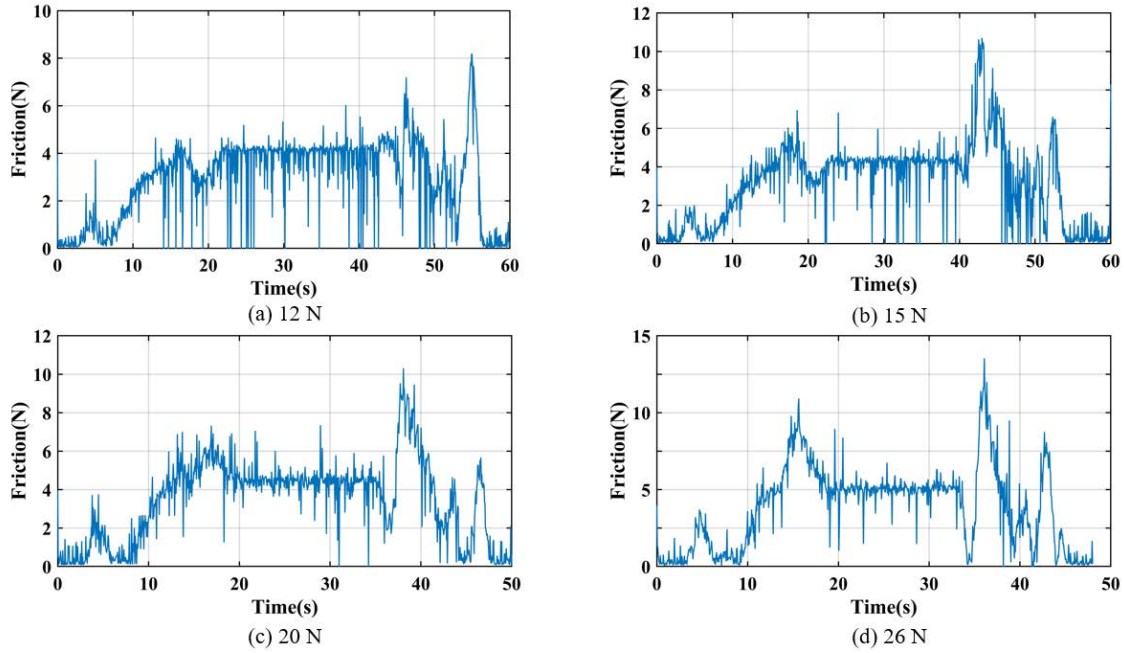

FIGURE 12. Friction changes of the driving wheel with different magnetic force.

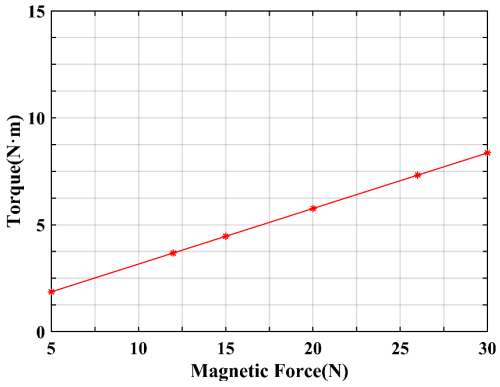

FIGURE 13. Torque required to separate the magnetic wheel from the pipe wall under different magnetic forces.

FIGURE 14. Magnetic wheel.

distance difference, and it can describe the degree to which the robot deviates from the center line of the pipe. In straight motion, the ideal situation is that both E_d and θ tend to zero. Therefore, when yaw occurs, the fuzzy controller needs to dynamically adjust the output to make the robot recover straight motion quickly.

Fuzzy control maps the system input to the fuzzy set, and determines the output through the rule base. In this study, E_d and θ are the inputs of the fuzzy controller, and the output U is differential value of the two driving wheels. Set the range of E_d to $[-150\text{mm}, 150\text{mm}]$, θ is $[-15°, 15°]$, and yaw to the left is positive along the direction of robot motion. The fuzzy fields of inputs and outputs are $[-3,3]$, and fuzzy sets are {NB, NM, NS, ZO, PS, PM, PB}. The quantization process realizes the scale transformation of the input, and the fuzzification obtains its membership degree. The membership functions are set to the triangular curve, as shown in Figure 17.

The establishment of rule base depends on control experience. Generally speaking, the yaw of the head has a greater impact. Therefore, when θ is large, no matter what the value of E_d is, the differential value of the two driving wheels should be increased to make the head return to normal quickly. When θ is small, the output is adjusted according to E_d.When both θ and E_d are very small, the control target is the stability of motion, so the output should be adjusted in a small range. The specific fuzzy rules are shown in Table 2. The output represents the left wheel speed minus the right wheel speed.

Defuzzification transforms the outputs obtained by reasoning into motor control quantity, which is realized by the center of gravity method. The final control quantity of the motor is a PWM signal with a pulse width of 1500us-2000us.

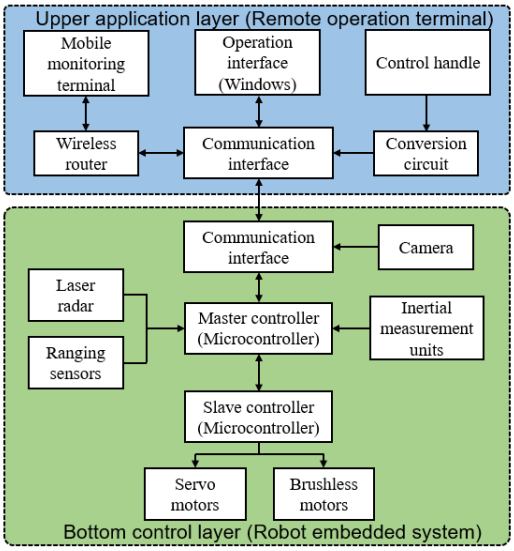

FIGURE 15. Control architecture of PR-I.

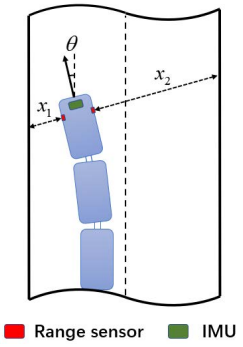

FIGURE 16. Posture of PR-I in straight motion.

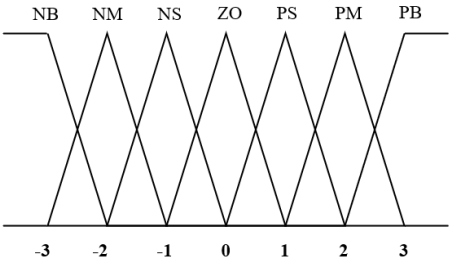

FIGURE 17. Triangular membership function.

2) TURNING

There is usually an initial differential value between the left and right driving wheels when turning. However, when unexpected interference occurs, turning failure is possible. A fuzzy controller for turning is proposed to make PR-I move along the middle arc curve in a bend. It is difficult for θ to describe the deviation of motion when turning, so the inputs of fuzzy controller are set to E_d and its change rate EC_d, and the range of EC_d is [−30,30]. The output should vary in a small range, so the differential value increment ΔU is used.

TABLE 2. Fuzzy rules for straight motion.

U		E_d						
		NB	**NM**	**NS**	**ZO**	**PS**	**PM**	**PB**
θ	**NB**	NS	NS	NM	NB	NB	NB	NB
	NM	ZO	ZO	NS	NM	NM	NB	NB
	NS	PS	ZO	ZO	NS	NS	NM	NM
	ZO	PM	PS	PS	ZO	NS	NS	NM
	PS	PM	PM	PS	PS	ZO	ZO	NS
	PM	PB	PB	PM	PM	PS	ZO	ZO
	PB	PB	PB	PB	PB	PM	PM	PS

The membership functions of input and output also choose triangular curves, and the fuzzy field is [−3,3].

The fuzzy rules are shown in Table 3. For ΔU,{NB, NM, NS} represents a reduction on the basis of the original differential value, {PB PM PS} means an increasement, and ZO means to keep the original differential value. Since the output is the differential value increment, turning fuzzy rules are universal for left and right turns. The difference is that E_d input values of left turn and right turn are opposite to each other during calculation.

TABLE 3. Fuzzy rules for turning.

ΔU		E_d						
		NB	**NM**	**NS**	**ZO**	**PS**	**PM**	**PB**
EC_d	**NB**	NB	NB	NB	NS	NS	ZO	PS
	NM	NB	NB	NM	NS	ZO	PS	PM
	NS	NB	NM	NM	ZO	PS	PM	PB
	ZO	NB	NM	NS	ZO	PS	PM	PB
	PS	NB	NM	NS	ZO	PS	PM	PB
	PM	NM	NS	ZO	ZO	PM	PB	PB
	PB	NM	NS	ZO	PS	PM	PB	PB

3) WALL CLIMBING

For wall climbing, the relationship between joint angle, angular velocity, robot centroid velocity and wheel velocity during the transition from horizontal pipe to vertical pipe is complex. More or less flexibility and passivity are effective in practical application. Therefore, the pitch joints of PR-I are free before the four units completely transition to the vertical pipe wall. After that, the pitch joints will provide a certain torque to reduce the influence of overturning moment. In addition, only the head and tail wheels of the robot provide driving force, and the magnetic force of the driving wheel decreases due to the covering of rubber film. Therefore, it is necessary to compensate the force through the pitch joint output. When slipping occurs, the acceleration of the robot is abnormal, which can be sensed by IMU. By adjusting the joint angle

slightly, the head and tail of the robot were pressed against the pipe wall to generate extra pressure, which can effectively improve the stability of wall climbing.

4) OBSTACLE SURMOUNTING

Terrain detection is realized by a TOF area array lidar installed on the head, and 8 × 8 resolution is sufficient for the special terrain inside the ventilation ducts. Each pixel provides depth and intensity information from 64 point cloud data, and terrain parameters can be calculated, such as the distance and height of obstacles. Step is the most common obstacle in the ventilation duct. The multi-link mechanism of PR-I requires gait planning when surmounting an obstacle. PR-I employs a travelling wave motion, and realizes obstacle surmounting by performing sequential control of a series of gaits, and they are implemented by programming trajectories of the joints in the bottom control layer. Three typical gaits in obstacle surmounting are shown in Figure 18.

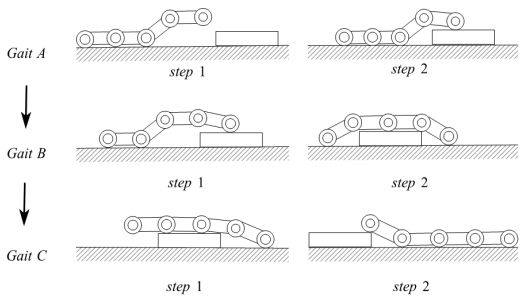

FIGURE 18. Gaits of obstacle surmounting.

Gait A (Lift head): Drive the pitch joints to lift the first two units, and move forward until the head crosses the obstacle. However, it is very difficult to lift two units at the same time due to the magnetic force, so lift the head first and then the second unit.

Gait B (Straighten back): This action will lift the two middle units, and forms a trapezoidal posture. This requires support from the head and tail. In other words, the wheels of the head and tail need to contact the pipe wall.

Gait C (Lift tail): Drive the tail pitch joint to lift the tail of the robot. At this time, the robot's center of mass is already above the obstacle. Moving forward and making the joints free, the robot can complete the obstacle surmounting.

The gaits can be applied to various obstacles with a height of less than 100mm. The yaw joints are locked to prevent lateral overturning. Obstacle surmounting is an autonomous process. When an obstacle is detected, the calculated distance and height information will be used for gait control, which determines the control quantity of joints and wheels. The magnetic encoder inside the servo motor module will provide joint angle feedback, and a simple PD controller is used to realize a more accurate angle control. Actually, the gait controller is a finite state machine. The next gait is never performed until the current gait reaches the desired posture.

V. EXPERIMENTS AND RESULTS

The performance test of PR-I was carried out in a real ventilation duct. The section size of the ventilation duct is 300mm × 300mm and the thickness is 1.2mm. Typical terrains such as straight pipe, vertical pipe, bend pipe and step obstacle were built.

A. STRAIGHT MOTION TEST

Straight motion requires no yaw when moving in a straight pipe. The initial posture of PR-I is described by a vector (x_1, x_2, θ). x_1 and x_2 are the detection values of the left and right range sensors of the head, and θ is the yaw angle, which is consistent with the parameters described in Figure 16. Several different initial postures were set to test the controller's performance, and the results are shown in Figure 19.

Figure 19(a) depicts the motion process with an initial posture of (48, 170, 0), which means that there was no head yaw initially, but the robot deviated to the left of the center line of the pipe. It can be seen that PR-I recovered the straight motion in about 3s, and remained stable after that. When the head yaw existed, as shown in Figure 19(b), PR-I eliminated the head yaw in about 1s, and moved along the center line of the pipe in about 3s. When the initial posture is (160, 76, −10), it can be seen from Figure 19(c) that when the head yaw and the deviation existed at the same time, the system had faster response. The yaw angle tended to zero within 0.5s, and the straight motion has been recovered at 1.5s. In Figure 19(d), an artificial disturbance was applied in about 0.8s. PR-I eliminated the yaw within 1s, then adjusted in a small range, and fully recovered the straight motion at 3.5s These results show that PR-I performs well in straight motion.

B. TURNING MOTION TEST

Consider two special initial postures to test turning performance, one is close to the inner wall of the pipe when turning left, and the other is close to the outer wall of the pipe when turning right. The experimental results are shown in Figure 20 (a) and (b) respectively.

In programming, when the head yaw angle changes by 90°, it is considered that the turning is completed. At this time, the yaw angle will be set to zero and enter the straight motion program. When turning left, the initial distance close to the left inner wall was 54mm, and when turning right, the distance close to the left outer wall was 38mm. In the two movements, the nearest distance between the robot and the pipe wall was not less than 30mm, and the turning was completed in about 2s. After that, it was adjusted by the straight motion fuzzy controller. It can be proved that the trafficability of turning can meet the requirements.

C. WALL CLIMBING TEST

PR-I can realize the horizontal-vertical-horizontal transition with a speed of 0.08m/s, and the climbing process is shown in Figure 21, which takes 43s. Figure 22 describes the change of motor torque during wall climbing movement. Due to the

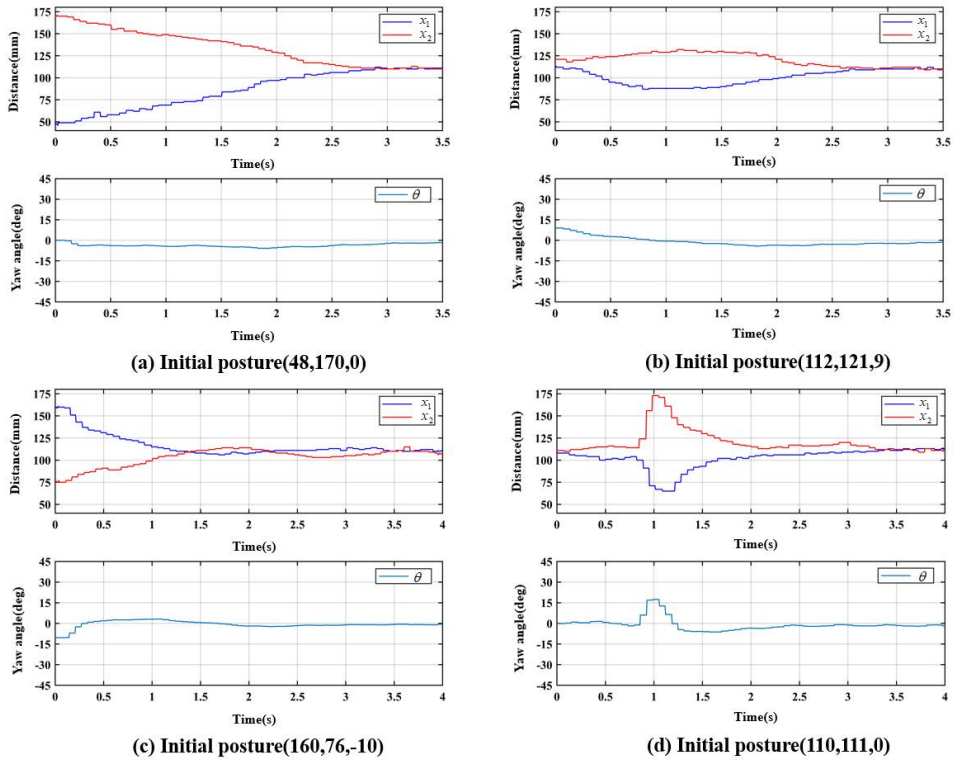

FIGURE 19. Straight motion experimental results under different initial postures.

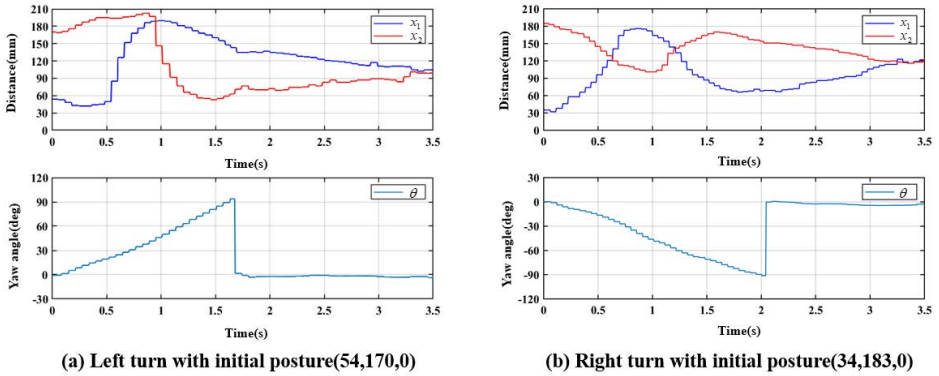

FIGURE 20. Turning experimental results.

lack of torque sensors, the torque is obtained by detecting the power according to $T_n = 9550P/N$. Where P is the power(kW), N is the speed(r/min). When T = 4s, PR-I moved to the curved pipe, and the torque of the driving wheel increased gradually. When PR-I climbed steadily on the vertical pipe wall (T = 20s to T = 30s), the torque was about 0.3N·m. When T = 30s, the robot began to transition to the horizontal pipe, and the torque of the driving wheel is reduced. Geometric constraints produce more resistance, so the final torque has a peak, which is consistent with the previous simulation results. When T = 43s, PR-I completed wall climbing process.

D. OBSTACLE SURMOUNTING TEST

The experiment of obstacle surmounting is shown in Figure 23, and the obstacle was a step with a height of 50mm and a length of 300mm. In order to ensure the stability of the overall movement, the joints and the wheels moved at a uniform speed. The motion characteristics are described by tracking the output power and angle changes of the joints, as shown in Figure 24 and 25 respectively. It can be seen from the output power changes that the maximum output of joint 1 occurred when the head was lifted (T = 1s), and the maximum output of joint 2 occurred when the first two units were lifted(T = 4s), which was due to the large

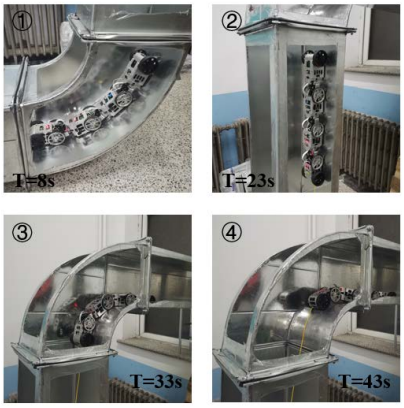

FIGURE 21. Wall climbing experiment.

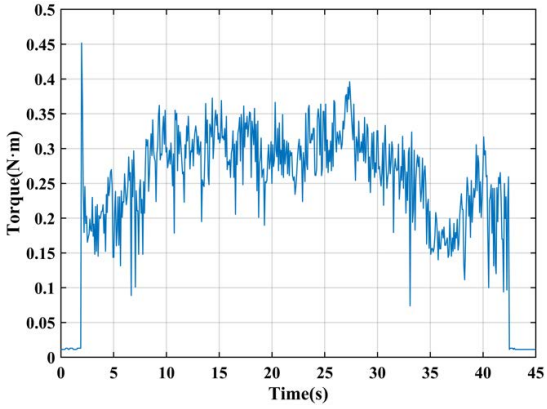

FIGURE 22. Torque variation curve of driving wheels.

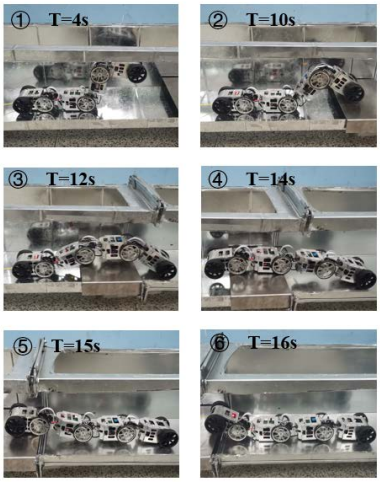

FIGURE 23. Obstacle surmounting experiment.

resistance caused by the separation of the magnetic wheel from the pipe wall. From T = 5s to T = 9s, PR-I moved forward until the head crossed the step, and the output of each joint remained relatively stable. When T = 10s, gait B was performed to lift the middle units, and the output of joint 2 and joint 3 increased. When T = 13s, the tail was

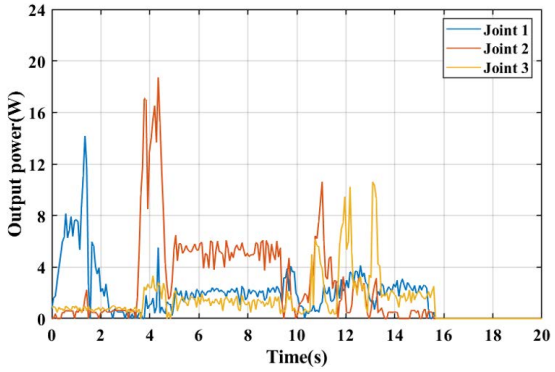

FIGURE 24. Output power variation curve of joints.

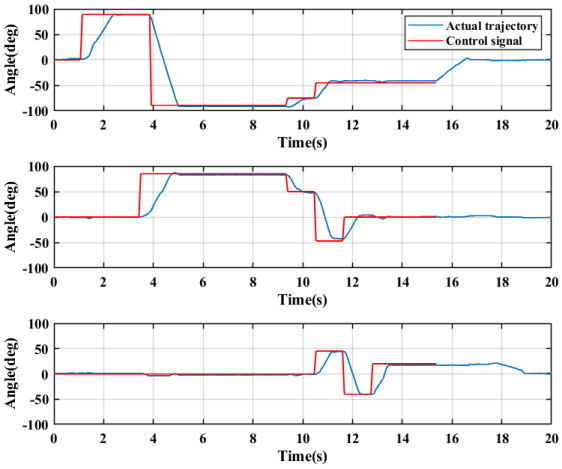

FIGURE 25. Joint angle trajectory curves.

lifted and the output of joint 3 reached another peak. When the tail crossed the step, all joints became free and moved passively, and the whole obstacle surmounting process lasted for 20 seconds. Step signals were used to control the joint angles. As can be seen from Figure 25, the closed-loop angle control has achieved a good performance, and the movement was relatively stable, and there was no excessive fluctuation.

VI. CONCLUSION

This paper proposed a multi-link magnetic wheeled pipeline robot PR-I, which has good trafficability in various terrains and can move freely in the ventilation ducts. A novel magnetic wheel is proposed, and the rectangular permanent magnets with different magnetizing directions are embedded in the wheels. The magnetic forces of several different arrangements are compared by finite element method. The optimal magnetic wheel structure is obtained through simulation analysis, and the magnetic force of the actual magnetic wheel is 13.9N.

The principle prototype and control system are developed, and different control algorithms and strategies are designed for different motion forms. The designed fuzzy controllers can keep the robot moving in a straight line, and recover

quickly when disturbed. When turning, it can improve trafficability and stability. A gait sequence is designed for obstacle surmounting, and its rationality and effectiveness are verified by experiments.

Motion tests show that PR-I has good control performance in straight motion, turning, wall climbing, and obstacle surmounting, and can meet the actual requirements. PR-I will be used for inspection, cleaning, and disinfection in the ventilation ducts, and the future work will be devoted to adding detection and cleaning devices to realize practical applications.

REFERENCES

[1] I. N. Ismail, A. Anuar, K. S. M. Sahari, M. Z. Baharuddin, M. Fairuz, A. Jalal, and J. M. Saad, "Development of in-pipe inspection robot: A review," in *Proc. IEEE Conf. Sustain. Utilization Develop. Eng. Technol. (STUDENT)*, Oct. 2012, pp. 310–315.

[2] L. Shao, Y. Wang, B. Guo, and X. Chen, "A review over state of the art of in-pipe robot," in *Proc. IEEE Int. Conf. Mechtron. Autom. (ICMA)*, Aug. 2015, pp. 2180–2185.

[3] Z. X. Li, H. W. Li, and Z. H. Li, "A new air-conditioning pipeline cleaning robot system," *Key Eng. Mater.*, vol. 464, pp. 313–317, Jan. 2011.

[4] F. S. Aureliano, A. A. F. Costa, and A. D. O. Lopes, "Cleaning and inspection of air conditioning ducts with rover explorer robot," *Proc. Manuf.*, vol. 17, pp. 350–356, Jan. 2018.

[5] F. Ito, T. Kawaguchi, M. Kamata, Y. Yamada, and T. Nakamura, "Proposal of a peristaltic motion type duct cleaning robot for traveling in a flexible pipe," in *Proc. IEEE/RSJ Int. Conf. Intell. Robots Syst. (IROS)*, Nov. 2019, pp. 6614–6621.

[6] H. Sawabe, M. Nakajima, M. Tanaka, K. Tanaka, and F. Matsuno, "Control of an articulated wheeled mobile robot in pipes," *Adv. Robot.*, vol. 33, no. 20, pp. 1072–1086, Oct. 2019.

[7] A. Kakogawa and S. Ma, "Design of a multilink-articulated wheeled pipeline inspection robot using only passive elastic joints," *Adv. Robot.*, vol. 32, no. 1, pp. 37–50, Jan. 2018.

[8] A. Kakogawa and S. Ma, "Design of a multilink-articulated wheeled inspection robot for winding pipelines: AIRo-II," in *Proc. IEEE/RSJ Int. Conf. Intell. Robots Syst. (IROS)*, Oct. 2016, pp. 2115–2121.

[9] A. Kakogawa and S. Ma, "An in-pipe inspection module with an omnidirectional bent-pipe self-adaptation mechanism using a joint torque control," in *Proc. IEEE/RSJ Int. Conf. Intell. Robots Syst. (IROS)*, Nov. 2019, pp. 4347–4352.

[10] Y. Oka, A. Kakogawa, and S. Ma, "A wheeled V-shaped in-pipe robot with clutched underactuated joints," in *Proc. IEEE Int. Conf. Robot. Autom. (ICRA)*, May 2021, pp. 13370–13376.

[11] C. Ye, S. Ma, H. Li, and J. Yang, "Development of a pipe cleaning robot for air conditioning system," in *Proc. IEEE Int. Conf. Robot. Biomimetics*, Dec. 2010, pp. 1525–1529.

[12] E. Dertien, M. M. Foumashi, K. Pulles, and S. Stramigioli, "Design of a robot for in-pipe inspection using omnidirectional wheels and active stabilization," in *Proc. IEEE Int. Conf. Robot. Autom. (ICRA)*, May 2014, pp. 5121–5126.

[13] H. Yan, L. Wang, P. Li, Z. Wang, X. Yang, and X. Hou, "Research on passing ability and climbing performance of pipeline plugging robots in curved pipelines," *IEEE Access*, vol. 8, pp. 173666–173680, 2020.

[14] A. Kakogawa, T. Nishimura, and S. Ma, "Designing arm length of a screw drive in-pipe robot for climbing vertically positioned bent pipes," *Robotica*, vol. 34, no. 2, pp. 306–327, Feb. 2016.

[15] G. Feng, W. Li, H. Zhang, Z. Li, and Z. He, "Development of a wheeled and wall-pressing type in-pipe robot for water pipelines cleaning and its traveling capability," *Mechanics*, vol. 26, no. 2, pp. 134–145, Apr. 2020.

[16] J. Chen, X. Cao, H. Xu, X. Zhang, and Z. Deng, "Structure design and characteristic analysis of compound-driven unit for pipeline robot," in *Proc. 5th Int. Conf. Adv. Robot. Mechtron. (ICARM)*, Dec. 2020, pp. 353–358.

[17] K. Huang, X. Li, Y. Sun, Y. Chen, M. Hao, and Y. Zhang, "Researches on a wall-climbing robot based on electromagnetic adsorption," in *Proc. 2nd Int. Conf. Intell. Manuf. Mater.*, 2018, pp. 644–647.

[18] J. Fan, T. Xu, Q. Fang, J. Zhao, and Y. Zhu, "A novel style design of a permanent-magnetic adsorption mechanism for a wall-climbing robot," *J. Mech. Robot.*, vol. 12, no. 3, Jun. 2020, Art. no. 035001.

[19] S. Hu, R. Peng, K. He, J. Li, J. Cai, and W. Zhou, "Structural design and magnetic force analysis of a new crawler-type permanent magnetic adsorption wall—Climbing," in *Proc. IEEE Int. Conf. Inf. Autom. (ICIA)*, Jul. 2017, pp. 598–603.

[20] C. Yan, Z. Sun, W. Zhang, and Q. Chen, "Design of novel multidirectional magnetized permanent magnetic adsorption device for wall-climbing robots," *Int. J. Precis. Eng. Manuf.*, vol. 17, no. 7, pp. 871–878, Jul. 2016.

[21] M. Tavakoli, C. Viegas, L. Marques, J. N. Pires, and A. T. de Almeida, "OmniClimbers: Omni-directional magnetic wheeled climbing robots for inspection of ferromagnetic structures," *Robot. Auton. Syst.*, vol. 61, no. 9, pp. 997–1007, Sep. 2013.

[22] F. Tache, W. Fischer, R. Siegwart, R. Moser, and F. Mondada, "Compact magnetic wheeled robot with high mobility for inspecting complex shaped pipe structures," in *Proc. IEEE/RSJ Int. Conf. Intell. Robots Syst.*, Oct. 2007, pp. 261–266.

[23] F. Tâche, W. Fischer, G. Caprari, R. Siegwart, R. Moser, and F. Mondada, "Magnebike: A magnetic wheeled robot with high mobility for inspecting complex-shaped structures," *J. Field Robot.*, vol. 26, no. 5, pp. 453–476, May 2009.

[24] R. Wang and Y. Kawamura, "A magnetic climbing robot for steel bridge inspection," in *Proc. 11th World Congr. Intell. Control Autom.*, Jun. 2014, pp. 11–17.

[25] R. Wang and Y. Kawamura, "An automated sensing system for steel bridge inspection using GMR sensor array and magnetic wheels of climbing robot," *J. Sensors*, vol. 2016, pp. 1–15, Dec. 2016.

[26] Y. Zhang, T. Dodd, K. Atallah, and I. Lyne, "Design and optimization of magnetic wheel for wall and ceiling climbing robot," in *Proc. IEEE Int. Conf. Mechtron. Autom.*, Aug. 2010, pp. 619–629.

[27] S. Gao, R. Hou, J. Li, Y. Pan, S. He, and H. Li, "Magnetic field analysis and structure design of a new magnetic wheel for wall-climbing robot," *J. Supercond. Novel Magn.*, vol. 35, no. 2, pp. 529–537, Feb. 2022.

[28] W. A. V. Stepson, A. D. I. M. Amarasinghe, P. N. R. Fernando, and Y. W. R. Amarasinghe, "Design and development of a mobile crawling robot with novel Halbach array based magnetic wheels," in *Proc. IEEE/RSJ Int. Conf. Intell. Robots Syst. (IROS)*, Sep. 2017, pp. 6561–6566.

[29] C. Park, J. Bae, S. Ryu, J. Lee, and T. Seo, "R-track: Separable modular climbing robot design for wall-to-wall transition," *IEEE Robot. Autom. Lett.*, vol. 6, no. 2, pp. 1036–1042, Apr. 2021.

MINGZE GAO received the B.S. degree in engineering from the School of Mechanical and Electrical Engineering, Beijing Information Science and Technology University, Beijing, China, in 2019.

He was at the Robotics Laboratory, Beijing Information Science and Technology University, from 2019 to 2022. Since 2019, he has been working with the research and development of pipeline robot system. His research interests include robot navigation and control.

MIN HUANG received the B.S. and M.S. degrees in engineering from the Nanjing University of Science and Technology, Nanjing, China, in 1987 and 1990, respectively, and the Ph.D. degree from the China University of Mining and Technology, Xuzhou, China, in 1997.

From 1997 to 2002, he was an Associate Professor at the China University of Mining and Technology, where he has been a Professor, since 2002. Since 2015, he has been the Dean of the School of Mechanical and Electrical Engineering, Beijing Information Science and Technology University. His research interests include robot intelligent perception and control and fault diagnosis of electromechanical equipment.

KAI TANG received the Ph.D. degree in engineering from the Beijing Institute of Technology, Beijing, China, in 2016.

From 2016 to 2019, he was as a Research Associate at the Beijing Institute of Technology. Since 2019, he has been an Associate Professor with the School of Mechanical and Electrical Engineering, Beijing Information Science and Technology University. He has been supported by the National Natural Science Foundation of China and the National Postdoctoral Science Foundation of China. His research interests include environmental perception and control and special robots.

XUQIANG LANG received the Ph.D. degree in engineering from Shandong Agricultural University, Taian, China, in 2014.

Since 2017, he has been a Lecturer with the School of Mechanical and Electrical Engineering, Beijing Information Science and Technology University. His research interests include robotics and mechatronics.

JIAMING GAO received the B.S. degree in engineering from Beijing Information Science and Technology University, Beijing, China, in 2019.

He was at the Robotics Laboratory, the School of Mechanical and Electrical Engineering, Beijing Information Science and Technology University, from 2019 to 2022. Since 2019, he has been working in the research and development of pipeline robot system. His research interests include robot structure design and simulation.